Simple, contrast based, compartmentalization in 3D reconstruction from CT images

A. S. Kussainov[1,2,*], N. O. Saduev[1,2], M. A. Em[1],
M. A. Mukhatay[1] and Y. T. Myrzabek[1]

[1]*Faculty of Physics and Technology, al-Farabi Kazakh National University,
71, al-Farabi Ave, 050040, Almaty, Kazakhstan*
[2]*National Nanotechnology Laboratory of Open Type, 71, al-Farabi Ave,
050040, Almaty, Kazakhstan*
*e-mail: arman.kussainov@gmail.com

We are interested in different procedures and techniques to preprocess and postprocess the data in computed tomography reconstruction methods to achieve the better contrast, resolution or other types of the functional analysis of the data. We report the straightforward application of the imaging artifacts treating technique, that is the elimination of the overexposure artifact due to the presence of the metal object, for producing the elementary image compartmentalization results with the artificial bone sample CT data. Thus, the high absorption artifacts removal technique is given the complimentary function of the structural analysis and revealing the metal pins scaffolding skeleton. The basic multilevel thresholding is used to reveal the targeted structures. The results could be extremely useful for the noisy, unfiltered X-ray source, single run data sets. The data have been supplied by the homemade CT scanner assembly and processed with the custom reconstruction software developed specifically for this setup. OpenCV package tools for the C/C++ libraries compiled with the MS Visual Studio IDE compiler were extensively used.

Key words: Computed tomography, thresholding, compartmentalization, FDK algorithm, backprojection, image reconstruction.
PACS number: 42.30.Wb.

1. Introduction

Computed tomography (CT) is mainly a medical imaging modality which uses the high penetration properties of the X-rays. The closest to it in its nature, produced results and analysis methods, are the projection radiographic imaging and X-ray mammography [1]. It has had found its way to the leading place in noninvasive medical diagnostics as well as to the multiple industry applications [2] such as searching for the defects, 3D modelling [3] and security applications [4].

Like every imaging techniques, dealing with the various types of materials, multitude of X-ray sources and detectors, CT has to address the numerous imaging artifacts appearing during the images acquisition stage, reconstruction procedure and data interpretation. The comprehensive list of theses artifacts is enormous [5] and generally assumes the additional efforts to preprocess and postprocess the images, introduction of the several

filtering techniques etc. Hardware-wise this may be the X-ray continuous spectrum filtering or the simple contrast-based procedures targeting the areas of different brightness or structural properties limited to the software methods.

With an advent of digital radiography, the matter became even more complicated [6]. One of the most common artifacts in all imaging techniques is caused by the limited bandwidth (discretization level) of the digital registration media/detectors [7]. That is if the registered image possesses the isolated spots of the extremely high/low luminosity and the detector is sensitized to include these high/low levels of intensities, but otherwise is limited in discretization value, the areas with the median value of brightness and low variations around this value will be overshadowed and may be completely obscured during resampling without the special treatment.

In our previous paper we demonstrated the regular approach to fix this contrast deficiency

artifact for the reconstructed images in our home-made computed tomography scanner application [8]. Although the grayscale, 16-bit (with 65536 shades of gray) discretization level, was enough to include the reasonable amount of graphical information about the sample inner structure together with the overexposed (underexposed) areas, such as metal objects within the sample, the human eye still percepts these images as an overall dim frames with the dominant dark/bright spot, see Figure 2(b).

The appearance of the metal objects with the high X-ray absorption properties whether as a deeply black or as a bright white spot is determined by a convention, according to which the high-density tissues and bones are shown as the white areas [9]. One could change it back by inverting the original absorption images and they will appear as the black unexposed areas on a film.

In this paper we used this effect as the simple image segmentation tool, see [10], though it could be addressed as the feature extraction tool [11] or even as a subclass of the fiber tracking problem [12].

Besides the ability to reconstruct the cross-section images from the sequence of the real data taken from the medical or experimental CT scanners, our software is capable to produce the full-scale CT simulation of the digital phantoms of high resolution and complex, user defined structure. This extends our ability to model the complex situations, filtering and reconstruction techniques.

2 Methods and Materials

The reconstruction algorithm which we used is based on the well-known method, called the FDK algorithm named after Feldkamp, Davis, and Kress, see [13]. The contemporary implementation of this algorithm with the extensive examples could be found in [14] and [15]. The FDK algorithm describes the backprojection of data from the multiple projections like $R_\beta(p,\varsigma)$ along the $f(t',s')$ tilted fans of rays, see Figure 1.

To begin with, the multiple images are taken from the sample by rotating the coupled X-ray source/detector around the sample. Next, the iterated summation of the pixel's intensity values to the some particular plane of interest, i.e. backprojecting from these X-ray images, will reproduce the original X-ray absorption properties distribution $g(t,s,z)$ in this plane. This process of backprojection, alongside with the basic filtration, is given by the next formula

$$g(t,s,z) = \frac{1}{2}\int_0^{2\pi} \frac{D^2}{(D-s)^2} \int_{-\infty}^{\infty} R_\beta(p,\varsigma) \cdot h\left(\frac{Dt}{D-s}-p\right) \frac{D}{\sqrt{D^2+\varsigma^2+p^2}} dpd\beta, \tag{1}$$

where D measures the distance from the source S to the point O on the axis of rotation. The p and ς values are the distance from the rotation axis and elevation of the current backprojecting ray relative to the tilted $f(t',s')$ fan's central ray s'. The $h(p)$ is produced by taking the inverse Fourier transform of $H(\omega)$, which is given by the following expression

$$H(\omega) = |\omega|b_\omega(\omega), \text{ where } b_\omega(\omega) = \\ = \begin{cases} 1, \text{ if } |\omega| < W \\ 0, \text{ if } |\omega| \geq W, \end{cases} \tag{2}$$

here W defines the window's size for the high-pass filter $H(\omega)$ in the Fourier space of the spatial frequencies ω, see [14].
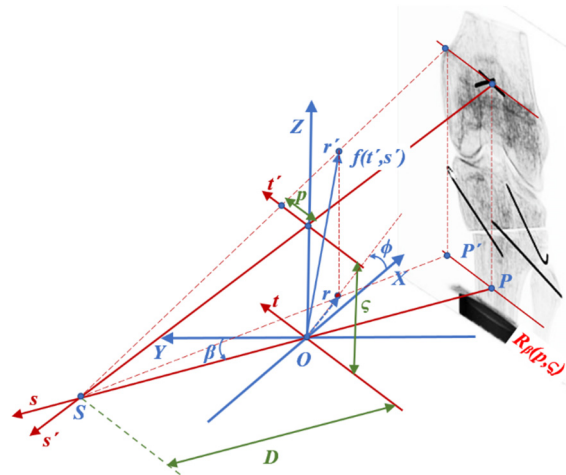

Figure 1 - The FDK backprojecting algorithm's basic geometry.

The coordinates (t,s) are fixed with respect to the rotated source-detector couple and related to the sample's static polar single plane frame of reference (r,ϕ) by the following obvious expressions

$$t = x \cdot cos(\beta) + y \cdot sin(\beta), \\ s = -x \cdot sin(\beta) + y \cdot cos(\beta), \tag{3} \\ x = r \cdot cos(\phi), y = r \cdot sin(\phi).$$

As the test data we used the images from an artificial polycarbonate tibiofemoral joint printed on the 3D printer. The G-297 Varex Imaging X-ray source and high resolution, 42.7 by 34.4 cm PaxScan

4336W v4 detector, were securely fixed relative to the lab while the sample, mounted on the rotation stage, was able to rotate freely in both directions in two degrees steps. The sample has the dimensions typical for the human tibiofemoral bones and after been projected takes the 18 by 12 cm area on the detector. The cone beam's geometry of the recording scheme assumes the double magnification of the sample if the distances between the source and the sample and between the sample and the detector were 140 and 70 centimeters correspondingly.

Four major parts of the joint, femur, patella (kneecap), tibia and part of the fibula, could be clearly seen on one of the sample projections, see Figure 2(a). The patella and the part of the fibula are attached to their main bones by the metal pins. In addition to this, the cap of the tibia is cut off and fixed back with the similar metal pins. We are aimed to build a method to extract this metal pins framework.

3 Results and Discussion

We used the variant of the global thresholding with the upper and lower limits imposed on the original data. Thus, depending on the limits, the metal pin image or the bone sample's structure only were allowed in the reconstructed image. The 50 coronal slices, occupying the shaded volume, see Figure 2(a), have been used for the procedure. The sample coronal slices before and after the metal pin image extraction are shown on Figures 2 (b) and (c) correspondingly.
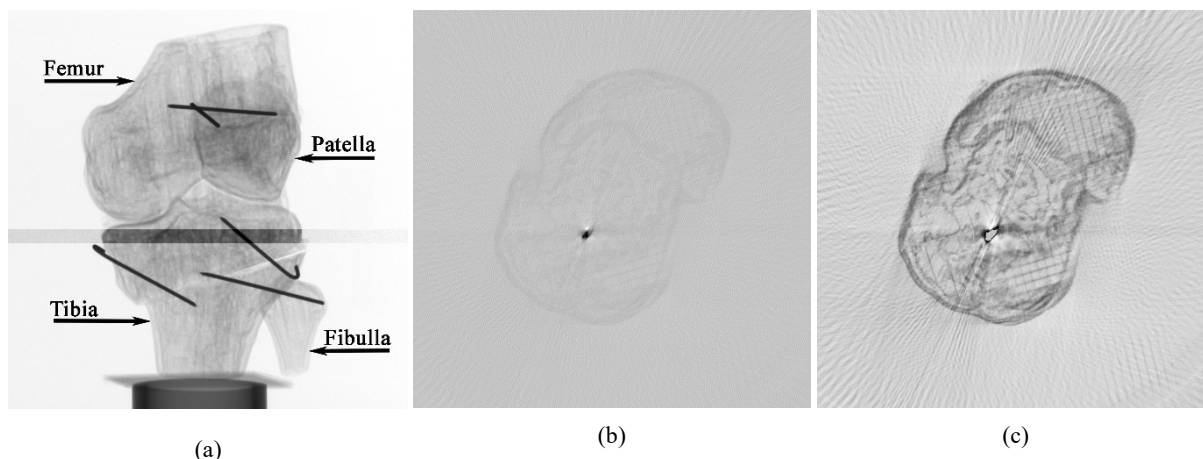

(a)

(b)

(c)

Figure 2 - (a) A single X-ray projection of the sample mounted on the rotation stage;
(b) Reconstructed coronal slice before the thresholding; (c) The same slice, see the previous
sub- figure, has the image of the metal pin extracted and intensity distribution fixed.

Each slice was exactly 5 voxels thick in order to achieve a uniform structure resolution across the field of view and get rid of the individual spontaneous imaging noise errors and artifacts typical for a single thin slice.

Adaptive mean and adaptive Gaussian thresholding were the few from the multitudes of methods available and considered in this study as well, see [16]. They were discarded, since we are not particularly concerned about extracting the true shape of the pin rather than about preserving the proper contrast across the images and studying the system of pins holding the whole assembly together.

Thus, the bi-level thresholding was used to build a mask M to extract the target features, metal pin image P or the bone sample's structure B, from an image A, according to the following model:

$$m_{ij} = 1 \text{ for } a_{ij} \geq T_1 \, ;$$
$$m_{ij} = 1 \text{ for } a_{ij} < T_2 \, ; \qquad (4)$$
$$m_{ij} = 0 \text{ for everything else} \, ,$$

where T_1 and T_2 are manually or semiautomatically selected for the range of images, see similar results in [17] and [18].

On the next figure, one can see the 3D images of the upper part of the femur and separately one of a metal shaft. Both were extracted from the data set according to the outline approach, see Figure 3(a) and (b).
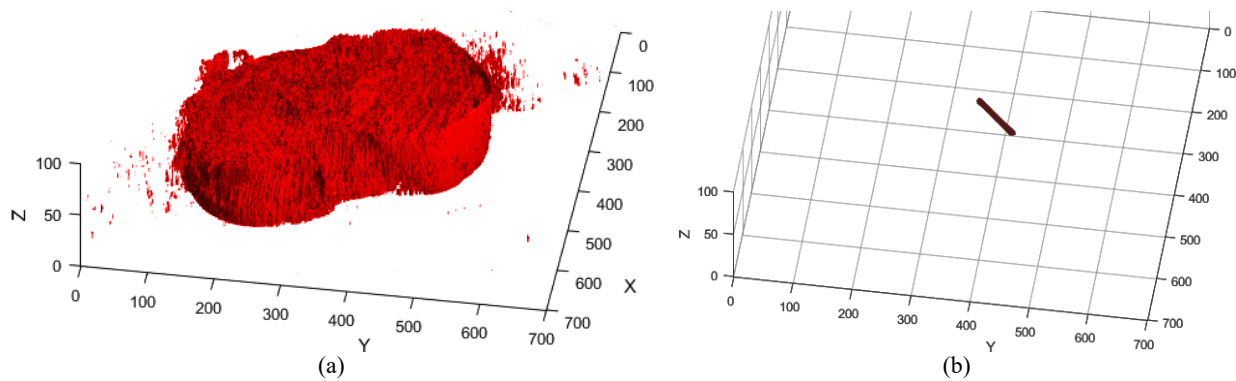
(a)   (b)

Figure 3 – 3D reconstruction of the upper part of the tibia. Based on the 50 slices, see Figure 2(c),
/with the metal pin images programmatically removed; (b) Reconstructed 3D image of the metal pin.
The set of the 50 slices, see Figure 2(b), after one level thresholding was used for the reconstruction.

In order to achieve the decent quality of the reconstructed images the multiple procedures with the extensive usage of OpenCV functions have been performed including but not limited to the adaptive ROI (region of interest) selection, image thresholding, image's features detection algorithm and homography transformation, see [19] and [20].

The data still look a little bit fuzzy because it was reconstructed from a single run, never repeated, set of images, with severe shift artifacts treated with our projection reconstruction software only. The work to optimize undersampled image reconstruction is underway [21].

Reconstruction and other simulation software are run on the personal computer with the 8-core Intel i7 4790K CPU and 32 Gb of RAM.

4 Conclusions

On the way of treating the most common imaging artifact, caused by a limited bandwidth of the detector/registration medium or by the multiple resampling, we implemented the simple contrast-based compartmentalization technique to extract the images of the metal pins holding the tibiofemoral joint sample together. The basic image processing and thresholding have been done in our reconstruction package by setting the proper values of brightness to be included into the reconstructed slices and using the other OpenCV image processing functions. The 3D reconstruction and data visualization from the set of backprojected slices are produced in Matlab.

Acknowledgements

References

1. Bushberg J.T., Seibert J.A., Leidholdt E.M., Boone J.M. The essential physics of medical imaging.-3rd ed.-Philadelphia, PA: Lippincott, Williams & Wilkins, 2012.-1030 p.

2. Flisch A. Industrial computer tomography in reverse engineering applications // Proceedings of the Computerized Tomography for Industrial Applications and Image Processing in Radiology Meeting. March 15-17, Berlin, Germany. -1999.- P.1.

3. Noel J. Advantages of CT in 3D scanning of industrial parts North Star imaging // 3D Scanning Technologies Magazine.-2008.-V.1. -No.3. -P.18.

4. Jin P., Haneda E., Sauer K.D., Bouman C.A. A model-based 3D multi-slice helical CT reconstruction algorithm for transportation security application // Second International Conference on Image Formation in X-Ray Computed Tomography.-Salt Lake City, Utah. -2012. –P.1.

5. Bell D.J., Shetty A. et al. X-ray artifacts.-Radiopaedia online resources. Accessed from https://radiopaedia.org/articles/x-ray-artifacts on November the 8th, 2020.

6. Walz-Flannigan A., Magnuson D., Erickson D., Schueler B. Artifacts in digital radiography. //American Journal of Roentgenology.-2012.-V. 198(1).-P.156-161.

7. Natterer F. The Mathematics of computerized tomography society for industrial and applied mathematic // Classics in Applied Mathematics. Philadelphia: SIAM, 2001.- 240 p.

8. Kussainov A.S., Saduev N.O. Homemade computed tomography setup with FDK reconstruction software // Journal of Physics: Conference Series.-2019.-V.1391.- P.012086.

9. Park H.S., Choi J.K., Seo J.K. Characterization of metal artifacts in X-Ray computed tomography // Communications on Pure and Applied Mathematics. - 2017.-V.70(11). -P.2191-2217.

10. Acharya T., Ray A.K. Image Processing - Principles and Applications.-USA:Wiley-Interscience, 2005.-452 p.

11. Kumar G., Pradeep B. A Detailed review of feature extraction in image processing systems // Proceedings of the IEEE Fourth International Conference on Advanced Computing & Communication TechnologiesAt: Rohtak, Haryana, India. -2014. –P.1.

12. Wieczorek M., Schaff F., Jud C. et al. Brain connectivity exposed by anisotropic X-ray dark-field tomography // Sci Rep.- 2018.- Vol.8. - P.14345.

13. Feldkamp L.A., Davis L.C., Kress J.W. Practical cone-beam algorithm // J. Opt.Soc. Am. A.-1984.-V.1.-P.612–619.

14. Kak A., Slaney M. Principles of computerized tomographic imaging (Society for Industrial and Applied Mathematics) // Prentice-Hall information and system sciences series, 2001.-323 p.

15. Jain A. Fundamentals of digital image processing // Prentice-Hall information and system sciences series (Prentice Hall), 1989.-569 p.

16. Sahoo P.K., Soltani S., Wong A.K., Chen Y.C. A Survey of thresholding techniques // Comput. Vision Graph. Image Process.-1988.-V.41.-P.233-260.

17. Quweider M.K., Scargle J., Jackson B. Grey level reduction for segmentation, thresholding and binarisation of images based on optimal partitioning on an interval // Image Processing, IET.-2007.-V.1(2).-P.103-111.

18. Otsu N. A threshold selection method from gray-level histograms // IEEE Transactions on Systems, Man, and Cybernetics.-1979.-V. 9.-No.1.-P.62-66.

19. OpenCV:Image Thresholding.-OpenCV (3.14.11-dev) online resources, accessed on October 30, 2020.

20. OpenCV:Feature Detection and Description.-OpenCV (3.14.11-dev) online resources, accessed on October 30, 2020.

21. Shen C., Lou Y., Chen L. et al. Comparison of three undersampling approaches in computed tomography reconstruction // Quant Imaging Med Surg.-2019.-V.9(7).-P.1229-1241.